Chemical Engineering Journal 163 (2010) 119–125

Contents lists available at ScienceDirect

Chemical Engineering Journal

journal homepage: www.elsevier.com/locate/cej

CFD analysis of a novel symmetrical planar SOFC design with micro-flow channels

Junxiang Shi, Xingjian Xue*

Department of Mechanical Engineering, University of South Carolina, Columbia, SC 29208, USA

ARTICLE INFO

Article history:
Received 26 April 2010
Received in revised form 7 July 2010
Accepted 9 July 2010

Keywords:
CFD model
SOFC
Bi-electrode supported
Micro-channel
Electrode design

ABSTRACT

This paper presents a novel design to mitigate fuel/gas feeding problem in bi-electrode supported cell (BSC) design. The traditional electrodes in BSC are replaced by the symmetrical electrodes notched with micro-channels to enhance fuel/gas flows while keeping the compact design of traditional BSCs. A three-dimensional mathematical model is developed to examine the performance of three BSC designs. Results indicate that the performances of the BSC with micro-channels (BSC-MC) are consistently better than those of BSC with homogeneous electrodes (homo-BSC) and BSC with heterogeneous electrodes (hetero-BSC). A prominent advantage of BSC-MC design is that it may obtain a very good performance under relative low fuel/gas pressure losses conditions through electrodes while homo-BSC and hetero-BSC require very high fuel/gas pressure losses in order to achieve comparable performances, which might be prohibited in practical SOFC systems.

1. Introduction

Solid oxide fuel cell (SOFC) has been widely recognized as one of promising clean energy conversion devices that convert the chemical energy of hydrogen into electrical energy directly. The fundamental structure of SOFCs is positive electrode-electrolyte-negative electrode (PEN) assembly, where the dense electrolyte is sandwiched by porous electrodes on either side. In recent years, tremendous efforts have been made towards the improvement of SOFC performance through various designs. Tubular and planar configurations are two classical designs and have been extensively investigated both experimentally and numerically in open literatures [1–6].

The tubular design has a seal-less feature and a good thermal shock resistance capability. However, the power density of this design is relatively low and the manufacturing cost is relatively high [7,8]. The planar design reaches another extreme; while it shows excellent manufacturability, and has high power density, the major hurdle with this design is the sealing problem [9–11]. Because the sealing materials are different from that of the cells, the thermal stress induced by the thermal expansion mismatch will lead to a series of problems. For instance, the thermal shock resistance capability is worse than that of the tubular design, which in turn leads to slow startup capability and less thermal cycle sustainability.

In order to overcome the drawbacks associated with the basic tubular and planar designs, many innovations have been made. In an attempt to avoid the long current path loss in traditional tubular SOFC design, a high power density SOFC (HPD-SOFC) design has been proposed, where the tubular geometric design has evolved into a flattened one with ribs in the electrode acting as bridges for current flow [12]. A novel 3D tubular type SOFC design has been developed by Koh et al. [13] to increase the active volumetric surface areas of the electrodes. The corrugated-shaped PEN plate design, which evolutes from basic planar PEN structure design and is known as mono-block layer built (MOLB) [14], may not only enhance the effective active area but also make the cell design compact. The combination of planar and tubular designs forms into the monolith type SOFC [15] by Murthy and Fedorov. Rolls-Royce developed an IP-SOFC design using multi-cell MEA concept [16], which takes advantage of both excellent thermal expansion compliance from tubular design and low cost component fabrication from planar design. Recently Cable and Sophie developed a novel design of symmetrical, bi-electrode supported cell (BSC) using freeze tape casting technique [17]. The BSC design has two remarkable features: the symmetrical structure provides more stable mechanical properties in thermal cycling conditions; fuel/gas flow channels are replaced by thick functionally graded porous electrode, thereby making the cell design more compact. However, this compact design imposes a great challenging on how to effectively feed fuel/gas due to the high diffusion resistance of porous electrodes.

In this research, a novel design is investigated, in which thick porous electrodes of BSC are notched with micro-channels as shown in Fig. 1. It is expected that the design with micro-channels will effectively enhance fuel/gas feeding without the need of high external gas pressures; meanwhile the new design still retains BSCs fundamental features of compactness and symmetry. The per-

---

* Corresponding author. Tel.: +1 803 576 5598; fax: +1 803 777 0106.
E-mail address: Xue@cec.sc.edu (X. Xue).

1385-8947/$ – see front matter. Published by Elsevier B.V.
doi:10.1016/j.cej.2010.07.031

Nomenclature

d_{pore}	Particle diameter in porous electrode (m)
d_p	Pore diameter in porous electrode (m)
D_{ij}	Binary mass diffusion coefficient of a mixture species i and j ($\mathrm{m^2\,s^{-1}}$)
D_{ij}^{eff}	Effective diffusion coefficient ($\mathrm{m^2\,s^{-1}}$)
$D_{\mathrm{Kn},i}$	Knudsen diffusion coefficient of species i ($\mathrm{m^2\,s^{-1}}$)
F	Faraday's constant: 96,487 ($\mathrm{C\,mol^{-1}}$)
h	Enthalpy
j_i	Current density ($\mathrm{A\,m^{-2}}$)
j_0	Exchange current ($\mathrm{A\,m^{-2}}$)
K	Permeability of porous electrode ($\mathrm{m^2}$)
M_{ij}	Mean molecular mass
M	Average molecular weight ($\mathrm{kg\,mol^{-1}}$)
n_i	Number fraction
N_t	Number density of all particles ($\mathrm{m^{-3}}$)
p	Pressure (Pa)
P_i	Probability for i phase particles to form percolated or globally continuous clusters
R	Universal gas constant ($\mathrm{J\,mol^{-1}\,K^{-1}}$)
S	Mass source term ($\mathrm{kg\,m^{-3}\,s^{-1}}$)
S_{TPB}	Volumetric reaction surface area ($\mathrm{m^{-1}}$)
S_h^e	Heat generation due to electrochemical reaction ($\mathrm{W\,m^{-3}}$)
S_h^j	Heat generation due to joule heating ($\mathrm{W\,m^{-3}}$)
S_i	Reaction source term for species i ($\mathrm{kg\,m^{-3}\,s^{-1}}$)
T	Temperature (K)
u	Velocity ($\mathrm{m\,s^{-1}}$)
V	Potential (V)
x	Direction parallel to electrolyte layer (m)
x_i	Mole fraction of species i
y	Direction perpendicular to electrolyte layer (m)
Z	Total average coordination number
Z_i	Total coordination for i phase particles

Greek symbols

α	Electron transfer coefficient (usually 0.5)
μ	Viscosity ($\mathrm{N\,s\,m^{-2}}$)
ρ	Density ($\mathrm{kg\,m^{-3}}$)
ω_i	Weight fraction of species i
η	Over-potential (V)
ϕ	Exchange potential (V)
γ	Reaction order for oxidation or reduction
κ	Ionic conductivity ($\mathrm{S\,m^{-1}}$)
σ	Electronic conductivity ($\mathrm{S\,m^{-1}}$)
π	Ratio of the circumference of a circle to its diameter
τ	Tortuosity
ε	Porosity

Subscripts

c	Cathode
a	Anode
i	Species *i*
ref	Reference
eq	Equilibrium
pol	Polarization
el	Electronic
io	Ionic

Superscripts

eff	Effective
e	Electrochemical reaction
j	Joule

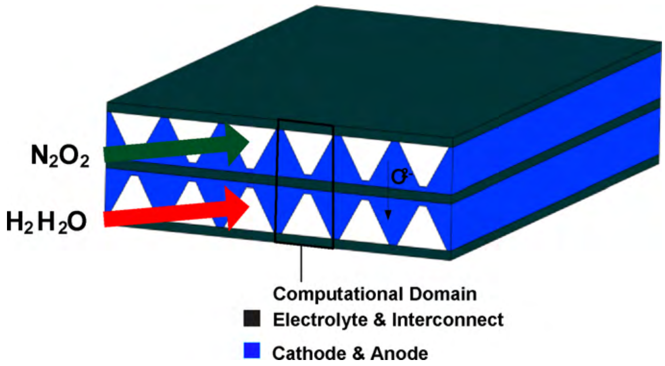

Fig. 1. Schematic of BSC with micro-channels.

formance of this new design is examined through mathematical modeling and numerical analysis.

2. Model description

Due to the periodic feature of the BSC structure shown in Fig. 1, a representative zone is chosen as a computational domain with cross-section details illustrated in Fig. 2. Essentially, the domain is composed of thin layer electrolyte sandwiched by symmetric electrodes on either side. The micro-channels notched in porous electrodes are utilized to enhance fuel/gas flow. Without loss of generality, we consider composite electrodes composed of electronic conducting particles, ionic conducting particles, and void phase. In the model development, it is also assumed that humidified hydrogen is used as a fuel, while air is used for cathode gas. A typical mathematical SOFC model, examining electrochemical, charge, flow, and thermal effects, considers the domains of cathode electrode layer, electrolyte layer, anode electrode layer as well as micro-channels, and includes the coupled processes of charge (ion/electron) balance, electrochemical reaction kinetics, mass balance, and momentum and energy balances. The model development is detailed in Tables 1 and 2 in order to save the space and keep conciseness.

2.1. Boundary conditions

The boundary conditions are needed to solve the coupled partial differential equations mentioned above, including inlet/outlet boundary conditions, continuity of flux, impermeability and no slip assumptions, etc., which are summarized in Table 3.

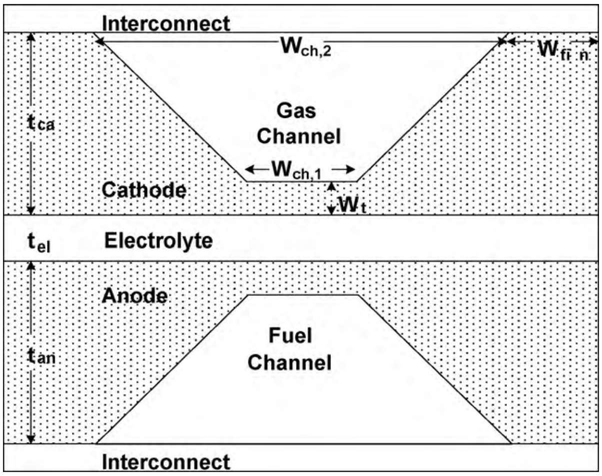

Fig. 2. Computational domain illustration of 2D cross-section.

Table 1
Mathematical model [19–22].

Governing equations	Mathematical expressions	
Charge balance (electronic)	$\begin{cases} \text{Anode electrode layer :} & \nabla \cdot \left(\sigma_{\mathrm{a}}^{eff} \nabla \phi_{\mathrm{e}}\right) = -j_{\mathrm{a}} S_{TPB} \\ \text{Cathode electrode layer :} & \nabla \cdot \left(\sigma_{\mathrm{c}}^{eff} \nabla \phi_{\mathrm{e}}\right) = -j_{\mathrm{c}} S_{TPB} \end{cases}$	(1)
Charge balance (ionic)	$\begin{cases} \text{Electrolyte layer :} & \nabla \cdot (\kappa \nabla \phi_i) = 0 \\ \text{Anode electrode layer :} & \nabla \cdot \left(\kappa_{\mathrm{a}}^{eff} \nabla \phi_i\right) = j_a A_V \\ \text{Cathode electrode layer :} & \nabla \cdot \left(\kappa_{\mathrm{c}}^{eff} \nabla \phi_i\right) = j_{\mathrm{c}} A_V \end{cases}$	(2)
Mass conservation	$\nabla \cdot \left(\rho u \omega_i - \rho \omega_j \sum D_i^{eff} \left(\nabla x_i + (x_i - \omega_j) \frac{\nabla p}{p}\right)\right) = S_i$	(3)
Momentum conservation (electrodes)	$\left(\frac{\mu}{K} + S\right) u = \nabla \cdot \left[-pI + \frac{\mu}{\varepsilon}\left(\left(\nabla u + (\nabla u)^T\right) - \frac{2}{3}(\nabla \cdot u) I\right)\right]$	(4)
Continuity (electrodes)	$\nabla \cdot (\rho u) = S$	(5)
Momentum conservation (channels)	$\rho(u \cdot \nabla) u = \nabla \cdot \left[-pI + \mu\left(\left(\nabla u + (\nabla u)^T\right) - \frac{2}{3}(\nabla \cdot u) I\right)\right]$	(6)
Continuity (channels)	$\nabla \cdot (\rho u) = 0$	(7)
Energy conservation (PEN, interconnects, channels)	$\nabla \cdot \left(k \nabla T + \sum_i h_i n_i\right) + \rho C_p u \cdot \nabla T = S_h^e + S_h^j$	(8)
	$\nabla \cdot (k \nabla T) = 0$	(9)
	$\nabla \cdot (k \nabla T) + \rho C_p u \cdot \nabla T = 0$	(10)

Table 2
Parameters associated with the model [19–22].

Effective ionic and electronic conductivities	$\kappa^{eff} = \kappa[(1-\varphi)(1-\varepsilon) P_{io}]^m$	(11)
	$\sigma^{eff} = \kappa[\varphi(1-\varepsilon) P_{el}]^m$	(12)
Percolation probability	$P_i = [1 - \left(\frac{4.236 - Z_{i-i}}{2.472}\right)^{2.5}]^{0.4}$	(13)
Coordination number	$Z = 6$	
	$Z_{i-j} = n_j \frac{Z_i Z_j}{Z}$	(14)
	$Z_{el} = 3 + \frac{Z - 3}{n_{el} - (1 - n_{el})(d_{io}/d_{el})^2}$	(15)
	$Z_{io} = 3 + \frac{Z - 3}{n_{el}(d_{el}/d_{io})^2 - (1 - n_{el})}$	(16)
Number fraction	$n_{el} = \frac{(d_{io}/d_{el})^3 \varphi_{el}}{1 - \phi_{el} + (d_{io}/d_{el})^3 \varphi_{el}}$	(17)
	$n_{io} = 1 - n_{el}$	(18)
Volumetric reactive surface area	$S_{TPB} = \pi \sin^2 \sin^2(\theta_c) N_t d_{el} d_{io} n_{el} n_{io} P_{io} P_{el} \frac{Z_{el} Z_{io}}{Z}$	(19)
Number density of all particles	$N_t = \frac{1 - \varepsilon}{(4\pi/3) d_{el}^3 (n_{el} + (1 - n_{el})(d_{io}/d_{el})^3)}$	(20)
Volumetric current densities	$j_a = j_{0,\mathrm{ref}}^{\mathrm{H_2}} \left(\frac{c_{\mathrm{H_2}}}{c_{\mathrm{H_2,ref}}}\right)^{\gamma_{\mathrm{H_2}}} \left[\exp\left(\frac{\alpha n F \eta_a}{RT}\right) - \exp\left(-\frac{(1-\alpha) n F \eta_a}{RT}\right)\right]$	(21)
	$j_c = j_{0,\mathrm{ref}}^{\mathrm{O_2}} \left(\frac{c_{\mathrm{O_2}}}{c_{\mathrm{O_2,ref}}}\right)^{\gamma_{\mathrm{O_2}}} \left[\exp\left(\frac{\alpha n F \eta_c}{RT}\right) - \exp\left(-\frac{(1-\alpha) n F \eta_c}{RT}\right)\right]$	(22)
Activation overvoltage	$\eta_i = \phi_{\mathrm{e}} - \phi_i - \Delta\phi_{\mathrm{eq}}$	(23)
Effective diffusion coefficient	$D_{ij}^{eff} = \frac{\varepsilon}{\tau}\left(\frac{D_{ij} D_{\mathrm{Kn},i}}{D_{ij} + D_{\mathrm{Kn},i}}\right)$	(24)
Binary diffusivity coefficient	$D_{ij} = \frac{0.00143 T^{1.75}}{p M_{ij}^{1/2} (V_i^{1/3} + V_j^{1/3})}$	(25)
Mean molecular mass	$M_{ij} = \frac{2}{(1/M_i) + (1/M_j)}$	(26)
Knudsen diffusion coefficient	$D_{Kn,i} = \frac{97}{2} d_{pore} \sqrt{\frac{T}{M_i}}, \quad d_{pore} = \frac{2}{3} \frac{\varepsilon}{1 - \varepsilon} d_p$	(27)
Average molecular weight	$M = \sum_{j=1}^{n} x_j M_j$	(28)
Density	$\rho = \frac{pM}{RT}$	(29)
Mass source term	$S = \sum_i \frac{j_i M_i}{n_i F}$	(30)
Permeability	$K = \frac{\varepsilon^3 d_p^3}{180(1 - \varepsilon)^2}$	(31)
Heat source terms	$S_h^e = (\Delta E_{elec\text{-}chem} - \Delta G) \frac{j}{n_i F}, \quad S_h^j = \sigma_{io} \varphi_{io}^2$	(32)

Table 3
Boundary condition settings in numerical computation.

Location	Boundary conditions (charge, mass, momentum, energy)
Cathode and gas channel inlet	$p = p_{out} + \Delta p_c, x_j = x_{j,ca,inlet}, T = T_{op}, \partial\phi_e/\partial x = 0$
Anode and fuel channel inlet	$p = p_{out} + \Delta p_a, x_j = x_{j,an,inlet}, T = T_{op}, \partial\phi_e/\partial x = 0$
Cathode and gas channel outlet	$p = p_{out}, \partial\phi_e/\partial x = 0, \partial x_j/\partial x = 0, \partial T/\partial x = 0$
Anode and fuel channel outlet	$p = p_{out}, \partial\phi_e/\partial x = 0, \partial x_j/\partial x = 0, \partial T/\partial x = 0$
Cathode and gas channel/interconnect	$\phi_e = V_{cell}, \partial x_j/\partial y = 0, u = 0, \partial T/\partial y = 0$
Anode and gas channel/interconnect	$\phi_e = 0, \partial x_j/\partial y = 0, u = 0, \partial T/\partial y = 0$
Cathode/electrolyte	$\partial\phi_e/\partial y = 0, \partial\phi_i/\partial y = 0, \partial x_j/\partial y = 0, \partial T/\partial y = 0, u = 0$
Anode/electrolyte	$\partial\phi_e/\partial y = 0, \partial\phi_i/\partial y = 0, \partial x_j/\partial y = 0, \partial T/\partial y = 0, u = 0$

3. Model validation

In order to perform high fidelity number analysis, the model needs to be validated using experimental data. Since the BSC with micro-channels is a new design concept, the corresponding experimental data is not available. On the other hand, the experimental data of NASA BSC is not publicly available either. In this paper, we will use the experimental data of home-made button cells to validate our model. The purpose of this validation is two folds: one is to examine our numerical code, another one is to determine the fundamental parameters associated with the model.

Experimental: The *V*–*I* curves for model validation were obtained using an in-house prepared cell. The powder mixture of NiO-$Ce_{0.9}Sm_{0.1}O_{1.9}$ (SDC) and organic additives were dry-pressed into a pellet as hydrogen electrode substrate. A layer of SDC powder was put on the surface of the substrate, co-pressed to form a bilayer structure consisting of anode electrode and electrolyte. The bilayer structure was then sintered at 1450 °C in air for 5 h. The $PrBa_{0.5}Sr_{0.5}Co_2O_{5+\delta}$ (PBSC) powders synthesized by a glycine–nitrate–process (GNP) were intimately mixed and ground with fine SDC powders and organic additives to form an ink, with which the SDC electrolyte surface of the SDC/NiO-SDC bilayer was painted and fired at 1250 °C for 2 h to form oxygen electrode. The obtained button cell has a diameter of 12 mm, oxygen electrode area of 0.35 cm^2, hydrogen electrode thickness of 400 μm, electrolyte thickness of 30 μm and oxygen electrode thickness of 50 μm, respectively. In the test, the mixture of 90 vol.% H_2 and 10% H_2O controlled by a precision flow meter (APEX) was used as a fuel, the ambient air as the oxidant. The corresponding *V*–*I* curves shown in Fig. 3 were recorded under different temperature conditions using Scribner 890EZ SOFC test system [18].

The mathematical model is solved using COMSOL Multiphysics 3.5. The physical parameters used in the model are summarized in Table 4. The parameters denoted by "a" are difficult to determine in the experiment and are used as adjustable parameters to fit the model predictions with experimental results. As shown in Fig. 3, the model predictions agree reasonably well with experimental data. While the model may need further validation for the novel BSC-MC designs, this task will leave for the future study when the corresponding experimental data is available.

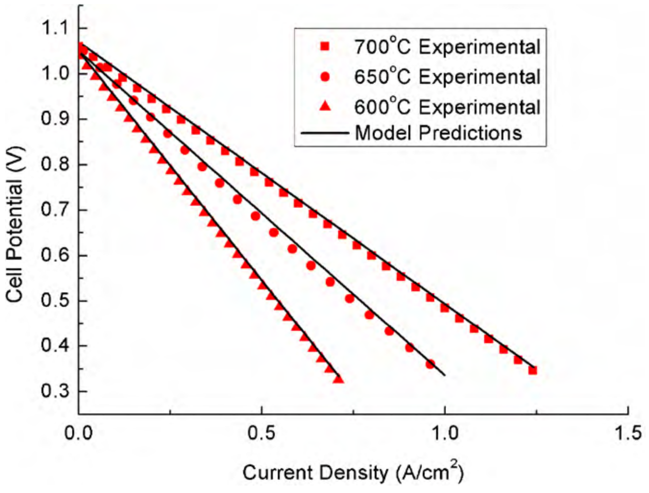

Fig. 3. Comparison between numerical results and experimental data.

4. Results and discussion

The mathematical model is then utilized to investigate BSC-MC performance and highlight the advantages of this novel design. As mentioned before, the potential problem with BSC design is on how to effectively feed fuel/gas while still keeping the compact designs. Here we compare three BSC designs, i.e., BSC design with homogeneous porous electrode (homo-BSC), NASA BSC with functionally graded porous electrode (hetero-BSC), and the novel BSC-MC design with notched micro-channels in homogeneous porous electrodes. The geometric dimensions of BSC-MC are shown in Table 5. In order to perform a fair comparison, the basic geometric dimensions of other two BSC designs are the same as those of BSC-MC, including the thicknesses of electrodes and electrolyte, as well as cell length and width.

Since the porous electrodes are functionally graded in NASA BSC design, the homogeneous porosity assumption is not applicable for mathematical model. However, the grading porosity can only be qualitatively observed from SEM [17], where the porosity has the maximum value at the electrode/interconnect interface while reaching the minimum value at the electrode/electrolyte interface,

Table 4
Parameters used for SOFC model validation [19–22].

Inlet temperature, T_{op} (°C)	600, 650, 700
Outlet pressure of electrodes, p_{out}(atm)	1.0
Fuel composition, $x_{H_2} : x_{H_2O}$	0.95:0.05
Air composition, $x_{O_2} : x_{N_2}$	0.21:0.79
Anode conductivity, σ (S/m)	$\left(9.5 \times \frac{10^7}{T}\right) e^{-(1150/T)}$
Cathode conductivity, σ (S/m)	$\left(4.2 \times \frac{10^7}{T}\right) e^{-(1200/T)}$
Electrolyte conductivity, κ (S/m)	$\left(3.34 \times \frac{10^4}{T}\right) e^{-(10,300/T)}$
Anode electrode layer thickness, t_{an} (μm)	400.0
Cathode electrode layer thickness, t_{ca} (μm)	50
Electrolyte thickness, t_{elec} (μm)	30
Porosity of anode and cathode, ε	0.35
Tortuosity of anode and cathode, τ[a]	3
Particle diameter, d_p (μm)	1
Contact angel between e^- and O^{2-} conducting particles, θ (°)[a]	30
Radius of e^- conducting particles, r_{el} (μm)	0.1
Radius of O^{2-} conducting particles, r_{io} (μm)	0.1
Volume fraction of e^- conducting particles, φ	0.5
Reference H_2 concentration, $c_{H_2,ref}$	10.78
Reference O_2 concentration, $c_{O_2,ref}$	2.38
Reaction order for H_2 oxidation, γ_{H_2}	0.5
Reaction order for O_2 reduction, γ_{O_2}	0.5

[a] Adjustable parameter.

Table 5
Parameters used for BSC-MC simulation [19–22].

Inlet temperature, T_{op} (°C)	800
Pressure loss of Anode's and Cathode's micro-channel (Pa)	20
Cell length and width (cm)	3 cm × 3 cm
Anode electrode layer thickness, t_{an} (μm)	2000
Cathode electrode layer thickness, t_{ca} (μm)	2000
Electrolyte thickness, t_{elec} (μm)	400
Micro-channel width, $W_{ch,1}$, $W_{ch,2}$ (μm)	1600, 200
Fin width (μm)	200
Porosity of anode and cathode, ε	0.3, 0.4, 0.5

the quantitative relationship is not available in open literature. In this work, an inverse parabolic function is utilized to simulate the graded porosity distribution in a statistical sense, as shown in Eq. (33),

$$f(y) = a\sqrt{y} + c \quad f \in [0.3, 0.6] \tag{33}$$

where a and c are constants and are used to determine the shape of porosity distributions; y is a variable defined as a distance between a point in an electrode and the corresponding electrode/electrolyte interface. It is worth noting that inverse parabolic porosity is utilized as an example for functionally graded electrode modeling, other distributions may also be applicable. The comprehensive study can be found in our recent paper [22].

4.1. Comparisons between traditional BSC designs and BSC-MC designs

For a fair comparison, the boundary conditions and operating conditions in the simulations are exactly the same for three BSC designs (as shown in Table 3). As an example, we set the cell voltage at 0.6 V, the corresponding hydrogen and oxygen concentration distributions in electrodes are shown in Figs. 4–6 for the designs of BSC with homogeneous electrodes, BSC with functionally graded electrodes, and BSC-MC, respectively. In other cell voltage conditions, hydrogen/oxygen concentration distributions show similar trends, which are omitted here due to space limitation. It is obvious to see from Figs. 4–6 that BSC-MC design obtains the most uniform concentration distribution among three designs. The BSC with functionally graded electrodes is a little bit better than BSC with homogeneous electrodes.

The cell performance comparisons under the same operating conditions are shown in Fig. 7, where the electrode porosity effects on cell performance are also investigated. Obviously the BSC-MC design demonstrates the best performance. Since notched micro-channels may effectively feed fuel/gas, the electrode porosity has little effects on BSC-MC performance. The homo-BSC design shows the worst performance and is significantly influenced by electrode porosities. With increasing porosity from 0.3 to 0.5, the fuel/gas feeding is enhanced; as a result, the cell performance is improved. The performance of hetero-BSC is between homo-BSC and BSC-MC. When hetero-BSC is operated in low current density conditions (less than 840 A/m^2 in this case), the performance of hetero-BSC is comparable to that of BSC-MC. Once the current density is beyond 840 A/m^2, hetero-BSC performance is worse than BSC-MC performance. In high current density conditions, the fuel/gas consumptions will be significantly increased. The high resistance of fuel/gas feeding in hetero-BSC design becomes the primary reason limiting the cell performance.

To highlight the effectiveness of fuel/gas feeding enhancement, BSC-MC performance is compared with that of hetero-BSC as shown in Fig. 8, where the cell voltage is set at 0.6 V as an example, the porosity of BSC-MC electrode is chosen as 0.4, the current density vs. cathode pressure loss is plotted. It is straightforward to see that hetero-BSC performance (current density) is significantly

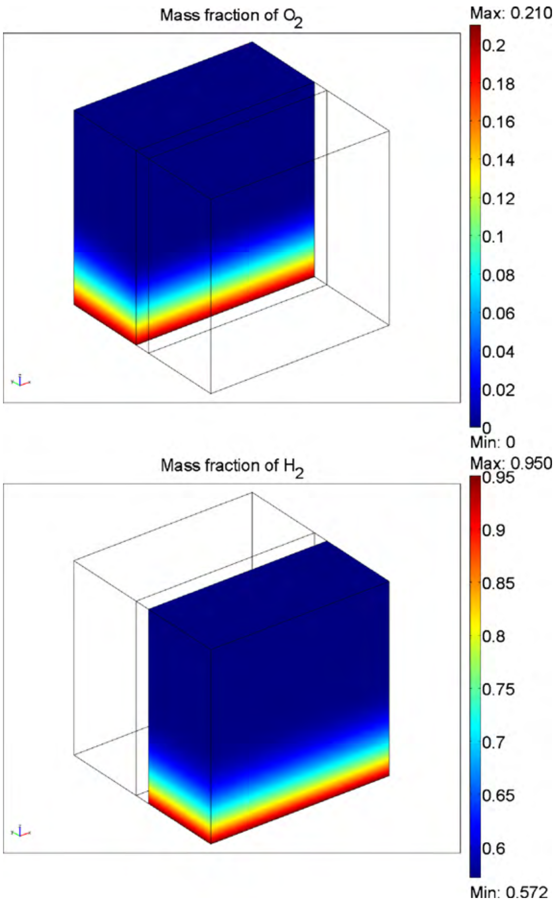

Fig. 4. Mass concentrations within homogeneous BSC.

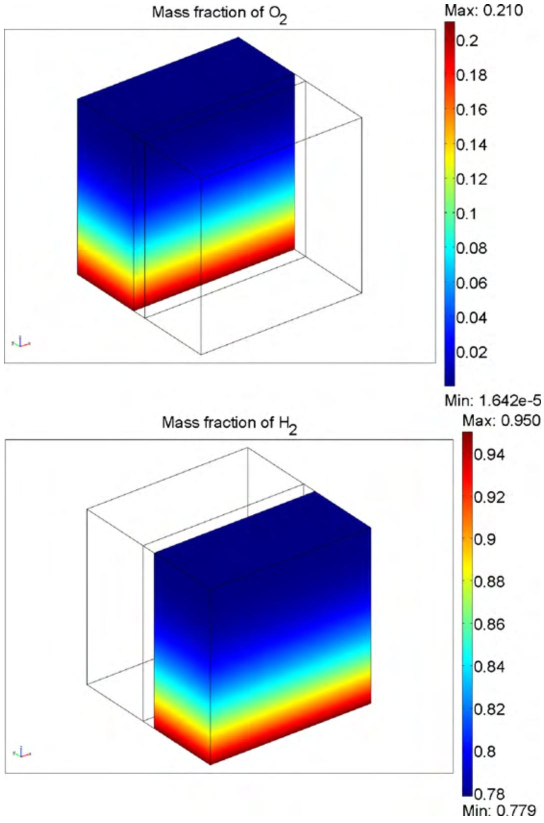

Fig. 5. Mass concentrations within heterogeneous BSC.

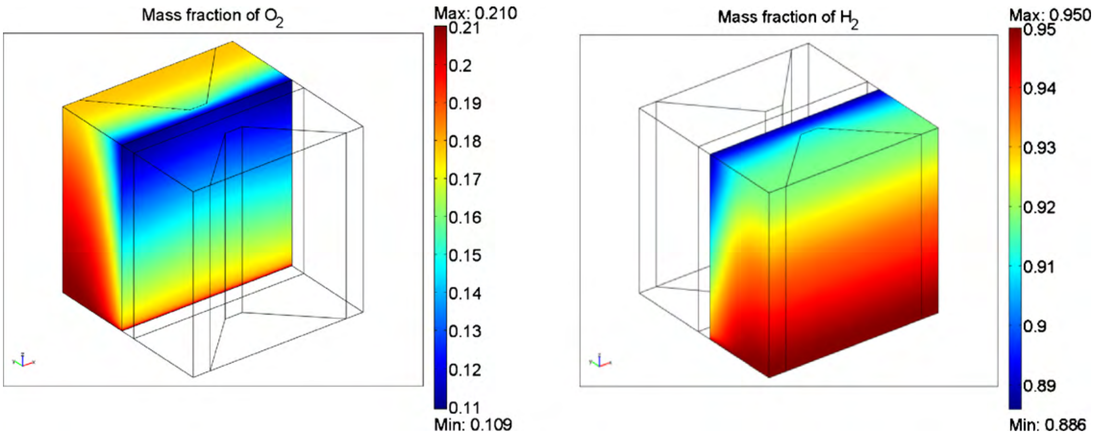

Fig. 6. Mass concentrations within BSC-MC.

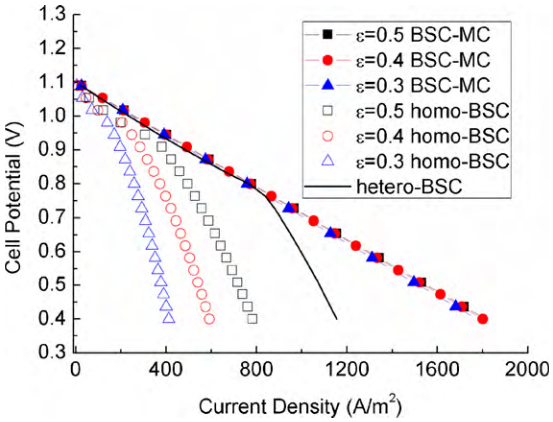

Fig. 7. Cell performances with different BSC designs.

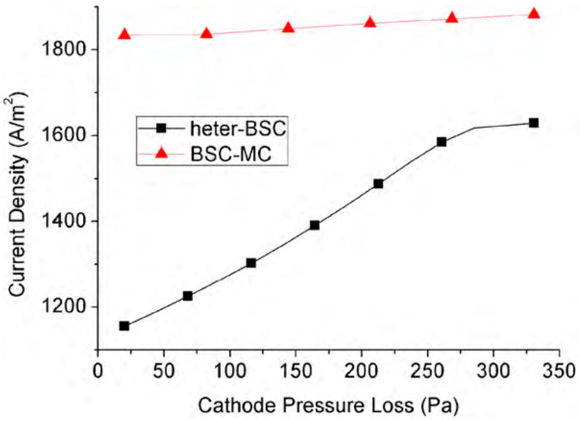

Fig. 8. Cell performance comparisons with different cathode pressure loss.

dependent on cathode pressure loss and increases with increasing cathode pressure loss, while BSC-MC performance just slightly influenced by cathode pressure loss. It is worth noting that BSC-MC performance is better than that of hetero-BSC under the same condition settings. These evidence indicate that the proposed BSC-MC design successfully solves the fuel gas feed problem, at the same time; it retains the advantages of the heterogeneous BSC design.

5. Conclusions

A comprehensive 3D CFD model is developed to investigate the novel design of BSC-MC. The model includes complicated interactions of mass/heat transfer, charge (electron and ion) migration, and electrochemical reactions. The model is validated using experimental data. Numerical results indicate that BSC-MC performance is comparable to hetero-BSC performance when the cell operating current density is low; both are better than homo-BSC performance. Under high current density conditions, the resistance of fuel/gas feeding through the electrode becomes a prominent issue for hetero-BSC. With notched micro-channels in electrodes, BSC-MC design successfully reduces fuel/gas feeding resistance through electrodes and shows much better performance than hetero-BSC and homo-BSC designs.

Acknowledgments

This work is supported by U.S. DOE under grant no. DE-SC0001061 through Energy Frontier Research Center (EFRC) titled “Science Based Nanostructure Design and Synthesis of Heterogeneous Functional Materials for Energy Systems”.

References

[1] S. Sunde, Monte Carlo simulations of conductivity of composite electrodes for solid oxide fuel cells, Journal of The Electrochemical Society 143 (3) (1996) 1123–1132.
[2] C.W. Tanner, K.-Z. Fung, A.V. Virkar, The effect of porous composite electrode structure on solid oxide fuel cell performance. 1. Theoretical analysis, Journal of The Electrochemical Society 144 (1) (1997) 21–30.
[3] E. Koep, C. Jin, M. Haluska, R. Das, R. Narayan, K. Sandhage, R. Snyder, M. Liu, Microstructure and electrochemical properties of cathode materials for SOFCs prepared via pulsed laser deposition, Journal of Power Sources 161 (1) (2006) 250–255.
[4] R.E. Williford, P. Singh, Engineered cathodes for high performance SOFCs, Journal of Power Sources 128 (1) (2004) 45–53.
[5] B.R. Roy, N.M. Sammes, T. Suzuki, Y. Funahashi, M. Awano, Mechanical properties of micro-tubular solid oxide fuel cell anodes, Journal of Power Sources 188 (1) (2009) 220–224.
[6] H. Zhu, A.M. Colclasure, R.J. Kee, Y. Lin, S.A. Barnett, Anode barrier layers for tubular solid-oxide fuel cells with methane fuel streams, Journal of Power Sources 161 (1) (2006) 413–419.
[7] H. Zhu, R.J. Kee, The influence of current collection on the performance of tubular anode-supported SOFC cells, Journal of Power Sources 169 (2) (2007) 315–326.
[8] X. Xue, J. Tang, N. Sammes, Y. Du, Dynamic modeling of single tubular SOFC combining heat/mass transfer and electrochemical reaction effects, Journal of Power Sources 142 (1–2) (2005) 211–222.
[9] H. Yakabe, T. Ogiwara, M. Hishinuma, I. Yasuda, 3-D model calculation for planar SOFC, Journal of Power Sources 102 (1–2) (2001) 144–154.
[10] K.P. Recknagle, R.E. Williford, L.A. Chick, D.R. Rector, M.A. Khaleel, Three-dimensional thermo-fluid electrochemical modeling of planar SOFC stacks, Journal of Power Sources 113 (1) (2003) 109–114.

[11] H.-C. Liu, C.-H. Lee, Y.-H. Shiub, R.-Y. Lee, W.-M. Yan, Performance simulation for an anode-supported SOFC using Star-CD code, Journal of Power Sources 167 (2) (2007) 406–412.

[12] Y. Lu, L. Schaefer, Numerical study of a flat-tube high power density solid oxide fuel cell. Part II. Cell performance and stack optimization, Journal of Power Sources 153 (1) (2006) 68–75.

[13] Y.-H. Koh, J.-J. Sun, W.-Y. Choi, H.-E. Kim, Design and fabrication of three-dimensional solid oxide fuel cells, Journal of Power Sources 161 (2) (2006) 1023–1029.

[14] J.J. Hwang, C.K. Chen, D.Y. Lai, Computational analysis of species transport and electrochemical characteristics of a MOLB-type SOFC, Journal of Power Sources 140 (2) (2005) 235–242.

[15] S. Murthy, A.G. Fedorov, Radiation heat transfer analysis of the monolith type solid oxide fuel cell, Journal of Power Sources 124 (2003) 453–458.

[16] P. Costamagna, A. Selimovic, M. Del Borghi, G. Agnew, Chemical Electrochemical model of the integrated planar solid oxide fuel cell (IP-SOFC), Chemical Engineering Journal 102 (2004) 61–69.

[17] T.L. Cable, S.W. Sofie, A symmetrical, planar SOFC design for NASA's high specific power density requirements, Journal of Power Sources 174 (1) (2007) 221–227.

[18] H. Ding, X. Xue, $PrBa_{0.5}Sr_{0.5}Co_2O_{5+\delta}$ layered perovskite cathode for intermediate temperature solid oxide fuel cells, Electrochimica Acta 55 (11) (2010) 3812–3816.

[19] M.M. Hussain, X. Li, I. Dincer, Mathematical modeling of planar solid oxide fuel cells, Journal of Power Sources 161 (2) (2006) 1012–1022.

[20] D.H. Jeon, J.H. Nam, C.-J. Kim, Microstructural optimization of anode-supported solid oxide fuel cells by a comprehensive microscale model, Journal of The Electrochemical Society 153 (2) (2006) A406–A417.

[21] S. Kakaç, A. Pramuanjaroenkij, X.Y. Zhou, A review of numerical modeling of solid oxide fuel cells, International Journal of Hydrogen Energy 32 (7) (2007) 761–786.

[22] J. Shi, X. Xue, CFD analysis of a symmetrical planar SOFC with heterogeneous electrode properties, Electrochimica Acta 55 (18) (2010) 5263–5273.